Microstructure, In Vitro Corrosion Behavior and Cytotoxicity of Biodegradable Mg-Ca-Zn and Mg-Ca-Zn-Bi Alloys

H.R. Bakhsheshi-Rad, E. Hamzah, H.Y. Tok, M. Kasiri-Asgarani, S. Jabbarzare, and M. Medraj

The effects of bismuth (Bi) addition on the microstructure and corrosion behavior of the Mg-Ca-Zn-Bi alloys were evaluated using electron microscopy, electrochemical test and electrochemical impedance spectroscopy. Microstructural observations showed that Mg-1.2Ca-1Zn-xBi (x = 0.5, 1.5, 3 wt.%) are composed of Mg_2Ca, $Ca_2Mg_6Zn_3$ and Mg_3Bi_2 phases while a new phase Mg_2Bi_2Ca appeared after the addition of 5 and 12 wt.% Bi to the Mg-1.2Ca-1Zn alloy. Furthermore, the additions of 0.5 wt.% Bi to the Mg-1.2Ca-1Zn alloy slightly improved the corrosion behavior of the alloy, while further increase in Bi amount from 1.5 to 12 wt.% has a deleterious effect on the corrosion behavior of the ternary Mg-1.2Ca-1Zn alloy which is driven by galvanic coupling effect. Cytotoxicity tests indicate that the Mg-1.2Ca-1Zn presents higher cell viability compared to Mg-1.2Ca-1Zn-0.5Bi alloy. In addition, the cell viability of both alloys increased with increasing incubation time while diluting the extracts to 50% and 10% improved the cell viabilities. The present results suggest that the Mg-1.2Ca-1Zn-0.5Bi can be interesting candidate for the development of degradable biomaterials and it is worthwhile for further investigation in an in vivo environment.

1. Introduction

The development of biomedical science field including tissue-implant interaction, tissue engineering and biomedical implant materials has given rise to the new concept of biodegradable biomaterials (Ref 1, 2). Unlike the conventional inert biomaterials, this kind of biomaterials is expected to promote beneficial interactions with the implant sites. Biodegradable materials are one of the best biomaterials within these bioactive biomaterials categories. These materials help the healing process of the damaged tissue during its gradual degradation. Eventually, they will fully degrade when the healing process is completed. Hence, unlike the other type of implants, no secondary removal procedure is necessary (Ref 3-6). Magnesium (Mg) as biodegradable material possesses high biocompatibility, biodegradability and non-toxicity providing a great potential for implant applications (Ref 7-9). Besides, Mg is the cofactor for many enzymes as well as it stabilized the

structures of DNA and RNA (Ref 7). A normal person's diet contains about 300 mg of magnesium per day (Ref 7, 10). Without sufficient Mg^{2+} in the body, muscular paralysis, hypotension, respiratory distress and cardiac arrest may occur (Ref 11). In addition, Mg shows good mechanical properties where its compressive yield strength and fracture toughness are closer to bone than other biomaterials including other metals, polymers and ceramic (Ref 10, 12, 13). However, the use of magnesium is hindered by its poor corrosion resistance which causes the mechanical properties of the implant to significantly decrease resulting in the inability of tissue to heal (Ref 5, 10, 12). Furthermore, Mg corrosion process involves evolution of hydrogen gas which accumulates in vivo adjacent to the implant. The H_2 gas and subsequent formation of hydrogen bubbles can noticeably impair other clinical applications of Mg (Ref 2, 5, 14). To address this problem, several researches have been conducted based on the alloying of Mg to improve its corrosion resistance (Ref 14, 15). However, due to the use of hazardous alloying elements, such as aluminum (Ref 10, 14), lithium or zirconium (Ref 13) alloys containing these elements are not suitable implant materials (Ref 16). Among the Mg alloy systems, Mg-Ca and Mg-Zn have shown a good combination of mechanical properties and corrosion behavior suitable for biomedical applications (Ref 7, 8, 17, 18). Calcium (Ca) is one of the most favorable alloying elements for Mg-based alloy. It is one of the most abundant minerals in human bones (Ref 19), and it is necessary for growth of human bones. It is also a necessary element in chemical signaling with cells (Ref 13). The Mg-Ca basically consists of two phases; α-Mg and Mg_2Ca. An intermetallic phase such as Mg_2Ca refines the microstructure of Mg and strengthens the alloy. However, addition of Ca higher than the solubility limited leads to the increase in corrosion rate due to the occurrence of galvanic corrosion between α-Mg and Mg_2Ca (Ref 18, 20, 21). It will also weaken the mechanical properties of Mg-Ca as the result

H.R. Bakhsheshi-Rad, M. Kasiri-Asgarani, and S. Jabbarzare, Advanced Materials Research Center, Department of Materials Engineering, Najafabad Branch, Islamic Azad University, Najafabad, Iran; E. Hamzah and H.Y. Tok, Department of Materials, Manufacturing and Industrial Engineering, Faculty of Mechanical Engineering, Universiti Teknologi Malaysia, 81310 Johor Bahru, Johor, Malaysia; and M. Medraj, Department of Mechanical Engineering, Concordia University, 1455 De Maisonneuve Blvd. West, Montreal, QC H3G 1M8, Canada and Mechanical and Materials Engineering Department, Masdar Institute, PO Box 54224, Abu Dhabi, UAE. Contact e-mail: rezabakhsheshi@pmt.iaun.ac.ir.

of the formation of coarser Mg₂Ca phase along the grain boundaries (Ref 13). Similar to calcium, zinc (Zn) is a nutritionally essential element in the human body. Zn is also a necessary component for over 200 various enzymes in the human body (Ref 22). Gu et al. (Ref 7) reported that the daily recommended intake of Zn is about 15 mg. The excess amount of Zn is usually excreted through urine. Zn also helps to increase age-hardening effect, grain refining and improves the castability (Ref 12, 14). Cai et al. (Ref 23) showed that formation of low amount of Mg-Zn decreases the corrosion rate, while the existence of high amount of Mg-Zn in a network structure can enhance microgalvanic corrosion. Addition of another low-cost element, bismuth (Bi), having less toxicity than other periodic table neighbors such as antimony to Mg-based alloys leads to increase the mechanical properties (Ref 3, 24). Absorbed Bi is excreted primarily through the urine, and its biological half-time for whole-body retention is about 5 days (Ref 3). It is not bio-accumulative, and purified Bi is used in antimicrobial and anticancer fields (Ref 3). The addition of Bi also shows significant influence on the corrosion behavior of Mg alloy due to the formation of the Mg₃Bi₂ (Ref 3). Bismuth compounds such as bismuth oxide, hydroxide, oxychloride, trichloride and nitrate do not indicate poisoning effect; therefore, they are used in the cosmetics and pharmaceuticals industry (Ref 25). Limited studies have been carried out on the in vitro biocompatibility and corrosion behavior of the Mg-Zn-Ca-Bi quaternary alloys with different amount of Bi. Wang et al. (Ref 26) showed that the addition of small amount of Bi to AZ80 magnesium alloy increases tensile strength and elongation, while further addition reversed the effect. However, there is a lack of information concerning the influence of Bi content on the microstructure, cytotoxicity and corrosion resistance of Mg-Ca-Zn and Mg-Ca-Zn-xBi (x = 0.5, 1.5, 3, 5, 12 wt.%) quaternary alloys. Therefore, in the present study, the microstructure, corrosion behavior and cytotoxicity of the ternary and quaternary alloys were investigated.

2. Experimental

Magnesium alloys were prepared by melting 99.9% pure magnesium ingots, pure zinc chips (99.9%), pure bismuth (99.99% Bi) and Mg-32%Ca master alloy. The materials were melted by electrical resistance furnace under an argon gas atmosphere in a mild steel crucible at 760 °C. The molten metal was maintained for around 45 min at the melting condition for stabilization. After stabilizing, molten metal with different Bi (0.5, 1.5, 3, 5, 12 wt.%) contents and a constant content of 1.2 wt.% Ca and 1 wt.% Zn were poured into mild steel molds which had been preheated at 400 °C accompanied with 30-s stirring process. The chemical compositions of the ternary Mg-1.2Ca-1Zn and quaternary Mg-1.2Ca-1Zn-xBi alloys obtained by ICP-AES are listed are listed in Table 1. Specimens of 15 mm × 10 mm × 10 mm were cut from the achieved alloys ingots, and the samples were then mechanically wet ground with 320 to 4000 SiC grit papers. Microstructure observation was performed using an optical microscope (Olympus BX60F5), and a scanning electron microscope (JEOL JSM-6380LA) equipped with energy-dispersive x-ray spectroscopy (EDS) analysis. An average grain size of specimens was determined from three micrographs using linear intercept

method according to ASTM standard E112-G6. X-ray diffractometry (Siemens-D500) was used for identifying the phases present in the specimens using Cu Kα line generated at 40 kV and 35 mA. The immersion test procedure was carried out based on the ASTM standard G31-72. The specimens were then immersed in a beaker containing 200 ml of Kokubo simulated body fluid (SBF). The Kokubo SBF was prepared according to the previously reported method (Ref 27). The SBF was not replenished during the testing period. The average pH value of the SBF from three measurements was recorded during the soaking experiment after every 24-h interval. The immersion tests were repeated at least once to check the reproducibility of the results. Corroded surfaces were analyzed using scanning electron microscopy and EDS following immersion testing. The hydrogen evolution rate of the specimens was also measured during the 240-h immersion period in Kokubo solution. A sample was immersed in a beaker, while a funnel was located over the samples to collect evolved hydrogen in a burette above the funnel. The hydrogen evolution rate was calculated in ml/cm²/day before renewing the solution, and the volume of the evolved hydrogen was measured with a graduated burette. For electrochemical tests, rectangular specimens with a surface area of 1 cm² were mounted in epoxy resin. The test was conducted at 37 °C in an open air glass cell containing 350 ml Kokubo simulated body fluid (SBF) solution with a pH of 7.44, using PARSTAT 2263 potentiostat/galvanostat (Princeton Applied Research). A three-electrode cell was used for potentiodynamic polarization tests. Saturated calomel electrode (SCE) was used as a reference electrode. The counter electrode was made of graphite rod, and the specimen was the working electrode. The samples were immersed in the SBF for 1 h prior to the electrochemical test to establish the open-circuit potential. All experiments were carried out at a constant scan rate of 0.167 mV/s and initiated at −250 mV below the open-circuit potential. The electrochemical impedance spectra (EIS) were measured over a frequency range of 1 Hz to 100 kHz, and the data were analyzed using the ZSimpWin software. EIS test was also performed using VersaSTAT 3 machine. Each electrochemical test was duplicated to examine the reproducibility of the results.

Murine calvarial preosteoblasts (MC3T3-E1) were used to evaluate the cytotoxicity of the Mg-1.2Ca-1Zn and Mg-1.2Ca-1Zn-0.5Bi alloys according to the ISO 10993-5 standard (Ref 28). The 0.5 wt.% Bi alloy was selected for this study because it showed the lowest degradation rate in SBF. Cells were culture in Dulbecco's modified Eagle's medium (DMEM) with 10% fetal bovine serum (FBS), 100 U/mL penicillin and 100 μg/mL streptomycin at 37 °C in a humidified atmosphere of 5% CO₂. The ratio of surface area of alloy samples to the extraction medium was 1 cm²/mL. The extract was then withdrawn, centrifuged and serially diluted (100, 50 and 10%) for the cytotoxicity test or, alternatively, refrigerated at 4 °C before the cytotoxicity test. The control groups involved the use of DMEM medium as negative control. Following the incubation of the cells in a humidified 5% CO₂ atmosphere at 37 °C for 2, 4 and 7 days, the extracts were removed. Cells were incubated in 96-well culture plates at 1 × 10⁴ cells/mL medium in each well and then cultured in DMEM with 10% FBS. Then the extracts were replaced by media, 10 μL 3-(4,5-dimethylthiazol-2-yl)-2,5-diphenyltetrazolium bromide (MTT) was added to each well for 4 h, and 100 μL formazan solubilization solution (10% SDS in 0.01 M HCl) was added in each well overnight in the incubator. The spectrophotometrical absorbance of both

Table 1 Chemical composition of the Mg-1.2Ca-1Zn -*x*Bi alloys

Alloy	Actual chemical compositions, wt.%						
	Fe	Ca	Zn	Bi	Cu	Ni	Mg
Mg-1.2Ca-1Zn	0.009	1.22	1.09	0.04	0.003	0.003	Bal.
Mg-1.2Ca-1Zn-0.5Bi	0.007	1.20	1.02	0.57	0.002	0.002	Bal.
Mg-1.2Ca-1Zn-1.5Bi	0.011	1.21	1.07	1.54	0.004	0.004	Bal.
Mg-1.2Ca-1Zn-3Bi	0.008	1.24	1.12	3.21	0.003	0.002	Bal.
Mg-1.2Ca-1Zn-5Bi	0.009	1.17	1.01	5.11	0.001	0.001	Bal.
Mg-1.2Ca-1Zn-12Bi	0.010	1.24	1.08	12.21	0.003	0.003	Bal.
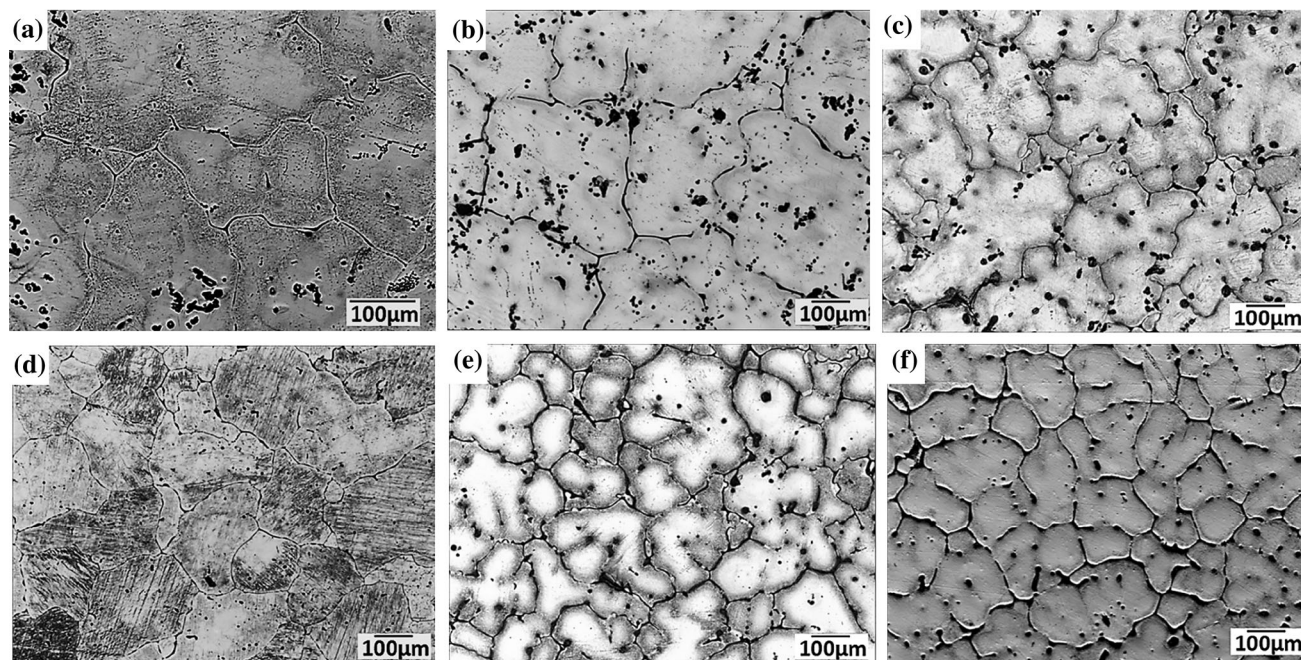
Fig. 1 Optical microscopic image of specimens (a) Mg-1.2Ca-1Zn and Mg-1.2Ca-1Zn-Bi alloys with various Bi content: (b) 0.5, (c) 1.5, (d) 3, (e) 5 and (f) 12 wt.%

alloys was measured at 570 nm by an automated microplate reader (Tecan Safire2).

3. Results and Discussion

3.1 Microstructure Characterization

The optical micrographs of the Mg-1.2Ca-1Zn and Mg-1.2Ca-1Zn-*x*Bi alloys (*x* = 0.5, 1.5, 3, 5 and 12 wt.%) are shown in Fig. 1. Figure 1(a) shows the Mg-1.2Ca-1Zn alloy with relatively large grain size which consisted of α-Mg matrix and traces of secondary intermetallic phases (dark area). Addition of 0.5 wt.% Bi slightly refined the grain size (Fig. 1b). Addition of Bi content up to 12 wt.% led to further grain refinement. The grain size for Mg-1.2Ca-1Zn alloy is 133 μm and decreases to 128 and 118 μm for Mg-1.2Ca-1Zn-0.5Bi and Mg-1.2Ca-1Zn-1.5Bi alloys, respectively (Fig. 1b, c). Further addition of Bi to 3 and 5 wt.% reduced the grain sizes from 118 to 93 μm and 87 μm, respectively (Fig. 1d, e). The smallest grain size was observed in Mg-1.2Ca-1Zn-12Bi alloy with 81 μm (Fig. 1f). Therefore, the growth restricted factor can be used to quantify the role of solute atoms in controlling the grain size. This has a direct relation with the slope of the binary liquids. Mg-Bi system has a liquidus line with higher gradient, $m = -1.67$ K/wt.%, than Mg-Ca system ($m = -6.53$ K/wt.%) and Mg-Zn ($m = -4.17$ K/wt.%) which indicates a higher ability for Bi to reduce the grain size of Mg alloy. Consequently, the Bi element increased the grain growth restriction when added to the Mg-1.2Ca-1Zn-*x*Bi alloy. This result explains the grain size reduction with increasing Bi content.

Figure 2 shows SEM micrographs of the Mg-1.2Ca-1Zn and Mg-1.2Ca-1Zn-*x*Bi alloys with different Bi content. Figure 2(a) and (b) shows that the ternary Mg-1.2Ca-1Zn consists of α-Mg, Mg_2Ca and $Ca_2Mg_6Zn_3$. The eutectic phases (α-Mg + Mg_2Ca + $Ca_2Mg_6Zn_3$) with lamellar structure formed within the grain boundaries. The EDS analysis further confirmed that the dark area is Mg_2Ca, and it is surrounded by the light area ($Ca_2Mg_6Zn_3$). The addition of Bi up to 3 wt.% in Mg-1.2Ca-1Zn leads to the precipitation of Mg_3Bi_2 intermetallic phases (light particles) within the grains in addition to α-Mg, Mg_2Ca and $Ca_2Mg_6Zn_3$ phases as can be seen in Fig. 2(e) and (f). It can be seen that most of Mg_3Bi_2 are formed around eutectic phases. The presence of these phases will be further confirmed by XRD analyses. The amounts of the Mg_3Bi_2

Table 2 Electrochemical parameters of Mg-1.2Ca-1Zn and Mg-1.2Ca-1Zn-xBi alloys in Kokubo solution obtained from the polarization test

Alloy	Corrosion potential, E_{corr}, mV/SCE	Corrosion current density, i_{corr}, μA/cm²	Cathodic slope, βc, mV/decade vs. SCE	Anodic slope, βa, mV/decade vs. SCE	Polarization resistance, Rp, kΩ cm²	Corrosion rate, Pi, mm/year
Mg-1.2Ca-1Zn	−1604 ± 14	164.0 ± 6	526.3 ± 21	122.9 ± 11	2.64 ± 0.06	3.75 ± 0.35
Mg-1.2Ca-1Zn-0.5Bi	−1576 ± 19	135.0 ± 5	619.7 ± 24	130.4 ± 13	3.47 ± 0.07	3.08 ± 0.32
Mg-1.2Ca-1Zn-1.5Bi	−1646 ± 15	220.7 ± 8	458.6 ± 18	154.8 ± 12	2.28 ± 0.05	5.04 ± 0.48
Mg-1.2Ca-1Zn-3Bi	−1681 ± 14	361.2 ± 10	396.2 ± 19	178.7 ± 10	1.48 ± 0.04	8.25 ± 0.65
Mg-1.2Ca-1Zn-5Bi	−1720 ± 17	423.0 ± 11	249.3 ± 17	122.8 ± 9	0.85 ± 0.02	9.67 ± 0.68
Mg-1.2Ca-1Zn-12Bi	−1778 ± 15	438.0 ± 11	135.7 ± 12	112.8 ± 12	0.61 ± 0.02	10.01 ± 0.71

intermetallic phase increased with increasing of Bi content up to 3 wt.% in the alloys as shown in Fig. 2(g) and (h). High amounts of Bi were found within the grain boundaries of Mg-1.2Ca-1Zn-3Bi, Mg-1.2Ca-1Zn-5Bi and Mg-1.2Ca-1Zn-12Bi alloys which indicates the existent of another intermetallic compound, Mg_2Bi_2Ca. In this case, the lamellar eutectic structure is composed of α-Mg, $Ca_2Mg_6Zn_3$ and Mg_3Bi_2 phases. Precipitate of Mg_2Bi_2Ca phases formed along and within the grain boundaries. Mg_2Bi_2Ca forms have a needle-like morphology which is distributed both within grains and along the grains boundaries. EDS analysis of area 6 shown in Fig. 2(l) further confirmed that these needle-shaped phases have an approximate composition of Mg-3Ca-1Zn-83Bi (wt.%).

Figure 3 shows the elemental mapping of the Mg-1.2Ca-1Zn and Mg-1.2Ca-1Zn-xBi alloy samples. The Mg-1.2Ca-1Zn sample was mostly composed of Ca and Zn in the lamellar structure which is surrounded by Mg (Fig. 3a). Elemental mapping of the Mg-1.2Ca-1Zn-0.5Bi and Mg-1.2Ca-1Zn-1.5Bi samples shows similar pattern as Mg-1.2Ca-1Zn with Bi element that distributed uniformly throughout the structure (Fig. 3b, c). The Bi and Ca contents concentrated within grains and along grains boundaries with further addition of Bi up to 12 wt.% (Fig. 3e, f) with needle-like structure heterogeneously distributed within the grain boundaries.

The XRD result of ternary Mg-1.2Ca-1Zn alloy shows the peaks of Mg, Mg_2Ca and $Ca_2Mg_6Zn_3$ phases (Fig. 4). Mg_2Ca has similar crystal structure as Mg which is hexagonal close packed (HCP) but with twice the lattice parameters $a = 0.623$ nm and $c = 1.012$ nm (Ref 29). The $Ca_2Mg_6Zn_3$ phase has hexagonal crystal structure with the lattice parameters $a = 50.97$ nm, $c = 51.00$ nm (Ref 30). By addition of 0.5-3 wt.% of Bi, the Mg_3Bi_2 phase shows relatively low intensity. With increase in Bi content in the specimens, the diffraction intensities of Mg_3Bi_2 phases also increase. Mg_3Bi_2 phase also has hexagonal crystal structure with lattice constants of $a = 0.466$ nm and $c = 0.733$ nm (Ref 3). By adding 5-12 wt.% of Bi, the peaks of Mg_2Bi_2Ca phase reflection were observed in addition to these of Mg_3Bi_2 and α-Mg.

3.2 Electrochemical Measurements

The results of the electrochemical test in Kokubo solution for Mg-1.2Ca-1Zn and Mg-1.2Ca-1Zn-xBi alloys are illustrated in Fig. 5. The Mg-1.2Ca-1Zn has more negative potential than Mg-1.2Ca-1Zn-0.5Bi alloy indicating that Bi has positive effect on the corrosion resistant of the alloys. The corrosion potential of Mg-1.2Ca-1Zn was −1.6040 V_{SCE}, and it shifted to more noble direction −1.576 V_{SCE} after the addition of 0.5 wt.% Bi into the alloy. The corrosion current density of Mg-1.2Ca-1Zn-0.5Bi alloy was 135.0 μA/cm², which is lower than Mg-1.2Ca-1Zn alloy (298.4 μA/cm²). This result shows that the secondary phase has a significant influence on the corrosion behavior of the alloy. Table 2 exhibits the electrochemical parameter of specimens obtained from the polarization curves. The corrosion potential shift to −1.646 V_{SCE} and the increase in corrosion current density to 220.7 μA/cm² have been observed after addition of 1.5 wt.% Bi in the ternary Mg-1.2Ca-1Zn alloy. Similar trend has been observed after the addition of 3, 5 and 12 wt.% Bi, as the corrosion potential become more cathodic to −1.681, −1.720 and −1.778 V_{SCE}, respectively. Also, corrosion current density increased to 361.2, 423.0 and 438.0 μA/cm², respectively. The
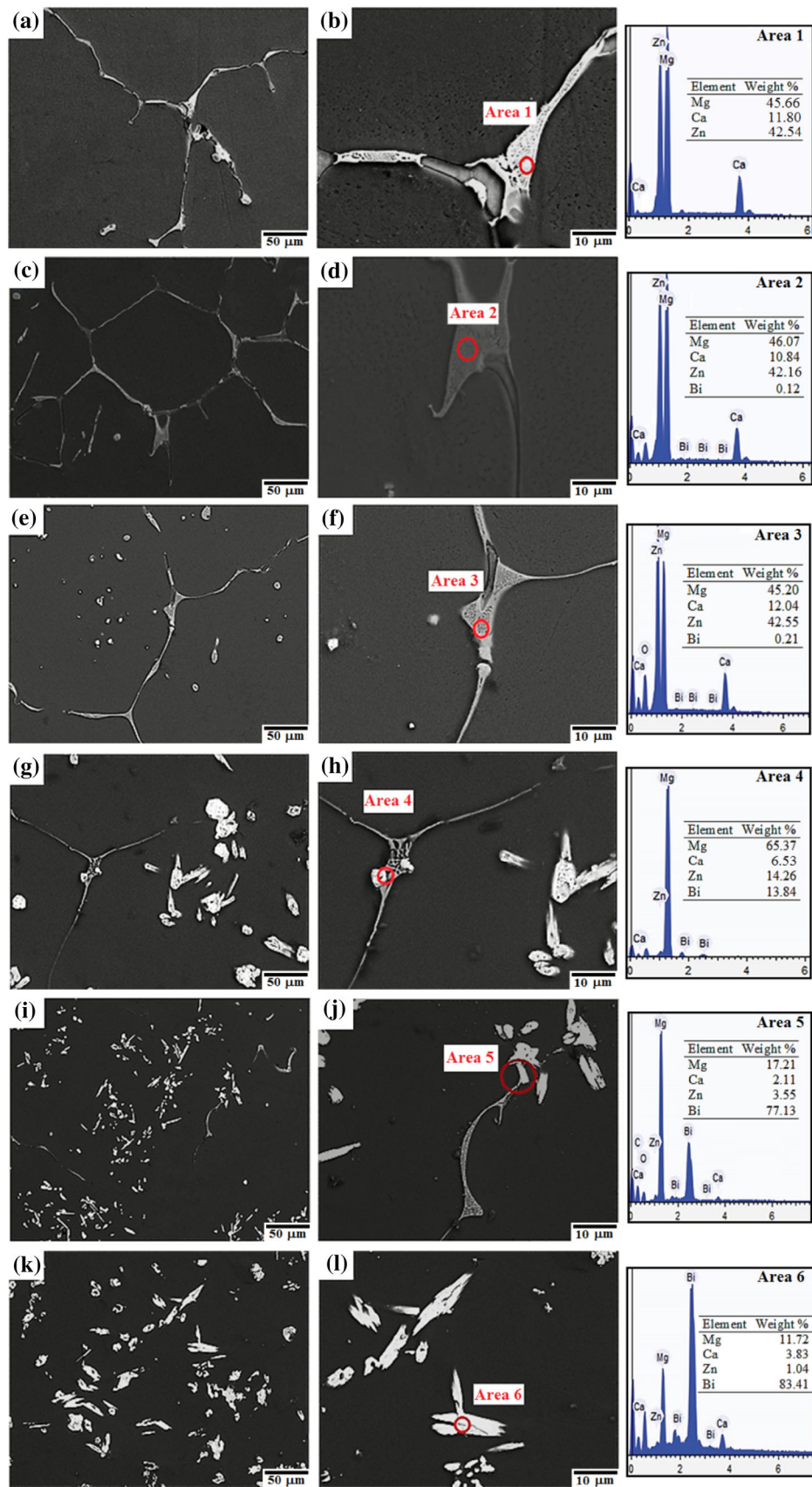
Fig. 2 SEM micrographs and corresponding EDX analysis of (a,b) Mg-1.2Ca-1Zn and Mg-1.2Ca-1Zn-Bi alloys with various Bi content: (c,d) 0.5, (e,f) 1.5, (g,h) 3, (i,j) 5 and (k,l) 12 wt.%
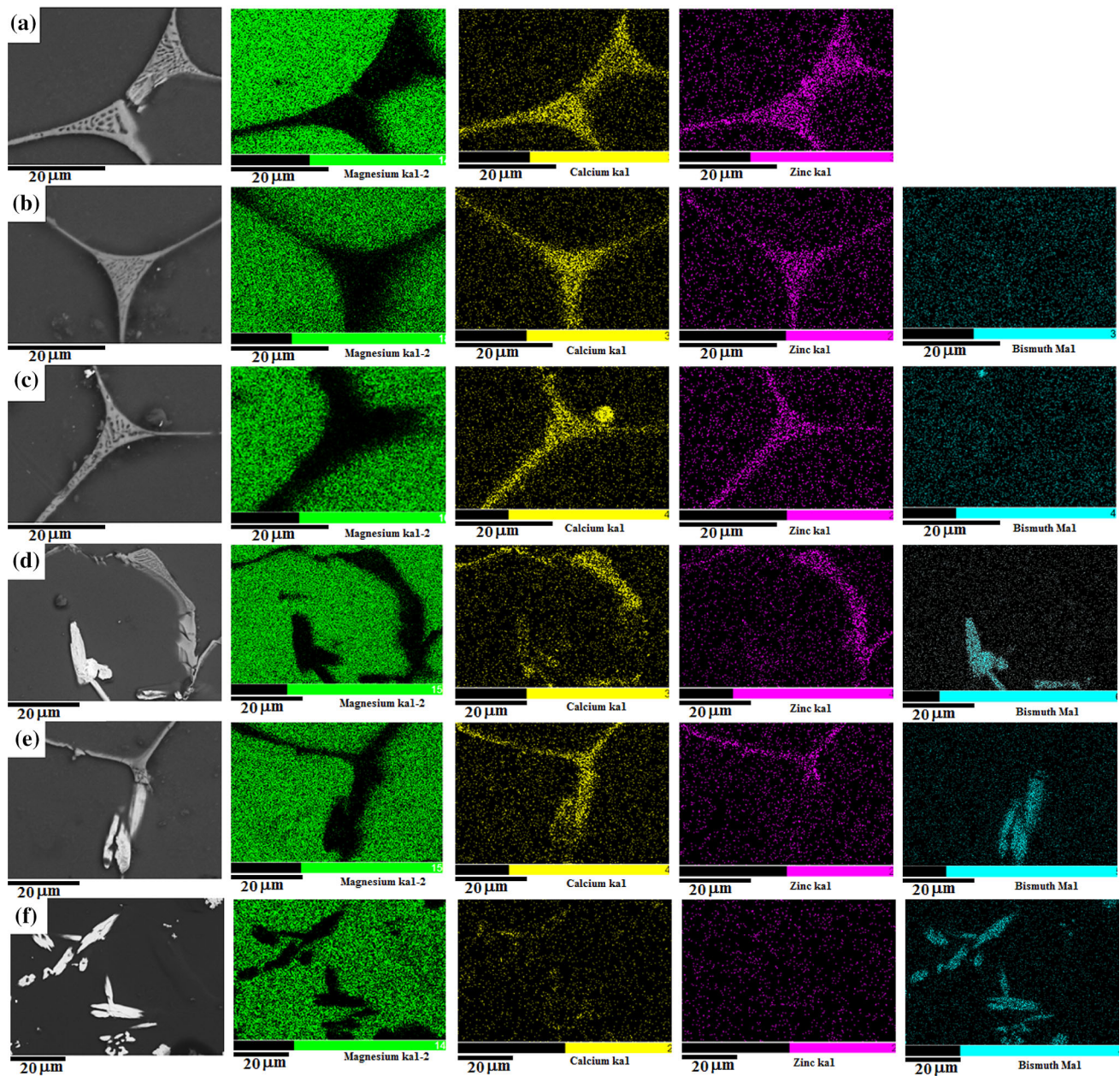
Fig. 3 Scanning electron micrographs and element mapping of (a) Mg-1.2Ca-1Zn and Mg-1.2Ca-1Zn-Bi alloys with various Bi content: (b) 0.5, (c) 1.5, (d) 3, (e) 5 and (f) 12 wt.%

result shows that Mg-1.2Ca-1Zn-0.5Bi alloy has lower corrosion resistance than other quaternary alloys having higher amount of Bi. It can be observed that the hydrogen evolution (cathodic polarization) in the Mg-1.2Ca-1Zn-0.5Bi was significantly higher than that of the Mg-1.2Ca-1Zn indicating that the corrosion potential (E_{corr}) was more negative in the alloy with small amount of Bi. The occurance of more galvanic corrosion between α-Mg and precipitated secondary phase has caused the reduction of corrosion resistance of the alloy (Ref 31, 32). The secondary phase acts as microcathodes which accelerate the corrosion of the quaternary Mg alloys when Bi content increased (Ref 18, 21). The presence of Mg_2Bi_2Ca phase and Mg_3Bi_2 in the alloy with high amount of Bi causes the occurrence of more galvanic potential between α-Mg (as anode) and Mg_3Bi_2 as cathode which results in decline of

corrosion resistance. Table 2 shows the corrosion potential (E_{corr}, V_{SCE}), current density (i_{corr}) and corrosion rate (P_i) of specimens obtained from the polarization curves. The corrosion rate P_i was calculated through the corrosion current density i_{corr} using Eq 1 (Ref 18, 33).

$$P_i = 22.85 i_{corr} \qquad \text{(Eq 1)}$$

The corrosion rate of the Mg-1.2Ca-1Zn was 3.75 mm/yr which are higher than that of Mg-1.2Ca-1Zn-0.5Bi alloy (3.08 mm/yr). However, the corrosion rate increased when the Bi content increased from 3 wt.% (5.04 mm/year) to 12 wt.% (10.01 mm/year). Moreover, the polarization resistance (R_p) was calculated from the electrochemical parameters (i_{corr}, β_a and β_c), according to Eq 2 (Ref 18).
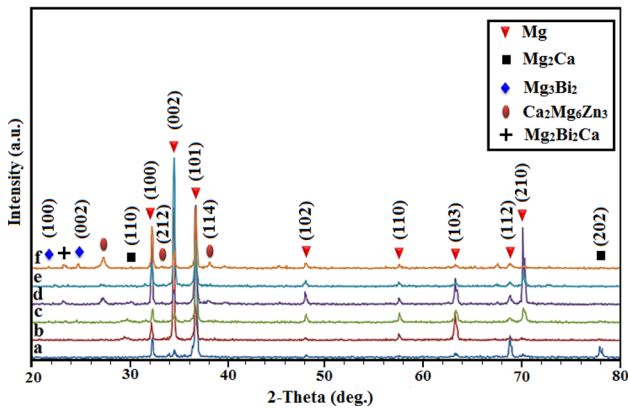
Fig. 4 X-ray diffraction patterns of (a) Mg-1.2Ca-1Zn and Mg-1.2Ca-1Zn-xBi alloys with various Bi content (b) 0.5 wt.%, (c) 1.5 wt.%, (d) 3 wt.%, (e) 5 wt.%, and (f) 12 wt.%
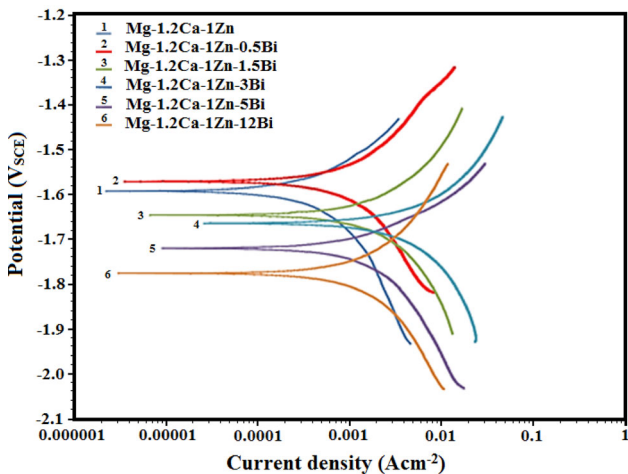

Fig. 5 Potentiodynamic polarization curves of the Mg-1.2Ca-1Zn and Mg-1.2Ca-1Zn-xBi alloys specimens in SBF at 37 °C

$$R_P = \frac{\beta_a \beta_c}{2.3 (\beta_a + \beta_c) i_{corr}}$$ (Eq 2)

The corrosion resistance of the Mg-1.2Ca-1Zn alloy improved as R_P values increased with the addition of 0.5 wt.% of Bi. However, further addition of Bi up to 12 wt.% has negative effect to the corrosion behavior of the alloy. The addition of 0.5 wt.% of Bi to Mg-1.2Ca-1Zn alloy increases the R_P from 2.64 to 3.47 kΩ cm^2. Further addition of Bi up to 12 wt.% significantly decreases the R_P from 3.47 to 0.61 kΩ cm^2. Therefore, the corrosion resistance of Mg-1.2Ca-1Zn-xBi improved with decreasing Bi content from 12 to 0.5 wt.%, and Mg-1.2Ca-1Zn-0.5Bi has better corrosion resistance than Mg-1.2Ca-1Zn alloy. It was due to the amount of Bi that dissolved in α-Mg matrix and precipitates formed as secondary Mg$_2$Bi$_2$Ca phase. The concentration of Bi dissolved in α-Mg matrix increases with the increased of Bi content in the alloys, and the excess Bi precipitates as secondary Mg$_2$Bi$_2$Ca phase. The higher Bi concentration in α-Mg, the Mg alloys exhibits better corrosion resistance. However, in the case of precipitation of Mg$_2$Bi$_2$Ca phase, the corrosion resistance decreases due to the occurrence of galvanic corrosion between α-Mg and secondary phase. Consequently, the solid solution of

Bi in α-Mg matrix can improve the corrosion resistance, while the precipitation of the secondary Mg$_2$Bi$_2$Ca phases reduces the corrosion resistance of the alloys.

Figure 6 shows SEM micrographs of the corroded surfaces of Mg-1.2Ca-1Zn and Mg-1.2Ca-1Zn-xBi alloys after electrochemical tests. Considerable areas of corrosion (dark area) were detected on the surface of Mg-1.2Ca-1Zn alloy (Fig. 6a). The addition of 0.5 wt.% is found to reduce the corroded area significantly (Fig. 6b). It is in good agreement with the result of electrochemical corrosion test. However, further addition of Bi content up to 12% increased the corroded area. The corroded area has fully covered the surface of specimen when the Bi content exceeds 12 wt.% and many pits are observed on the surface of the quaternary Mg-1.2Ca-1Zn-12Bi alloy (Fig. 6f). There were some sites left uncorroded (around grain boundary) due to the microgalvanic corrosion between the secondary intermetallic phases with the α-Mg phase where the α-Mg phase always acts as cathode. Those areas were in favor of localized corrosion attack. The surface of Mg-1.2Ca-1Zn-0.5Bi alloy was quite uniform and only composes of small area of corrosion. It further proved that it has more resistance to protect the alloy from the penetration of the solution compared to other specimens. Electrochemical impedance spectra (EIS) measurements for the Mg-1.2Ca-1Zn and Mg-1.2Ca-1Zn-xBi alloys were taken at open-circuit potential (E$_{ocp}$) as shown in Fig. 7(a). In general, the high corrosion potential and charge transfer resistance and low corrosion current density indicate that the test specimen has good corrosion resistance (Ref 34). As can be seen, the impedance diagram of the ternary and quaternary Mg-1.2Ca-1Zn-xBi alloys is characteristic of one well-defined capacitive loop which is attributed to the relaxation process of electrochemical reaction impedance corresponding to the dissolution of Mg and electric double-layer capacitance (C$_{dl}$) at the interface between the sample surface and corrosion medium (Ref 35). Thereby, the electrode reaction process correlated with high-frequency capacitive loop can be described by a parallel circuit of C$_{dl}$ and charge transfer resistance R$_t$ (Ref 23). The diameter of the high-frequency semicircle gives the charge transfer resistance R$_t$ at the electrode/electrolyte interface. Therefore, charge transfer resistance could be used to evaluate the corrosion property of the alloys. This is because the larger the R$_t$ is, the more difficult is the transfer of charges between solution and the sample surface, and thus the corrosion rate is low (Ref 23). As can be seen, the whole specimens show similar EIS spectra, except for the difference in the diameter of the capacitive loop. This indicated that the corrosion mechanism of aforementioned alloys is similar, while their corrosion rate is different. The EIS spectra of the entire samples can be fitted well using a simple equivalent circuit to characterize the samples where R$_e$ represents the solution resistance, C$_c$ is the coating capacitance and R$_{ct}$ is the charge transfer resistance. The graph shows that addition of Bi more than 0.5 wt.% Bi leads to a decrease in the diameter of the capacitive loop which means a decrease in corrosion resistance. Higher R$_t$ value obtained with addition of 0.5 wt.% Bi and the lowest value with 5 and 12 wt.% Bi addition reflects the alloy behavior during corrosion. This suggests that the addition of 0.5 wt.% Bi to ternary Mg-1.2Ca-1Zn alloy can hinder the charge transfer process at the substrate/electrolyte interface. The Bode plots of the EIS spectra obtained for the both ternary and quaternary samples are shown in Fig. 7(b). The impedance modulus at low frequency ($|Z|_{f=1Hz}$) is used to characterize the corrosion
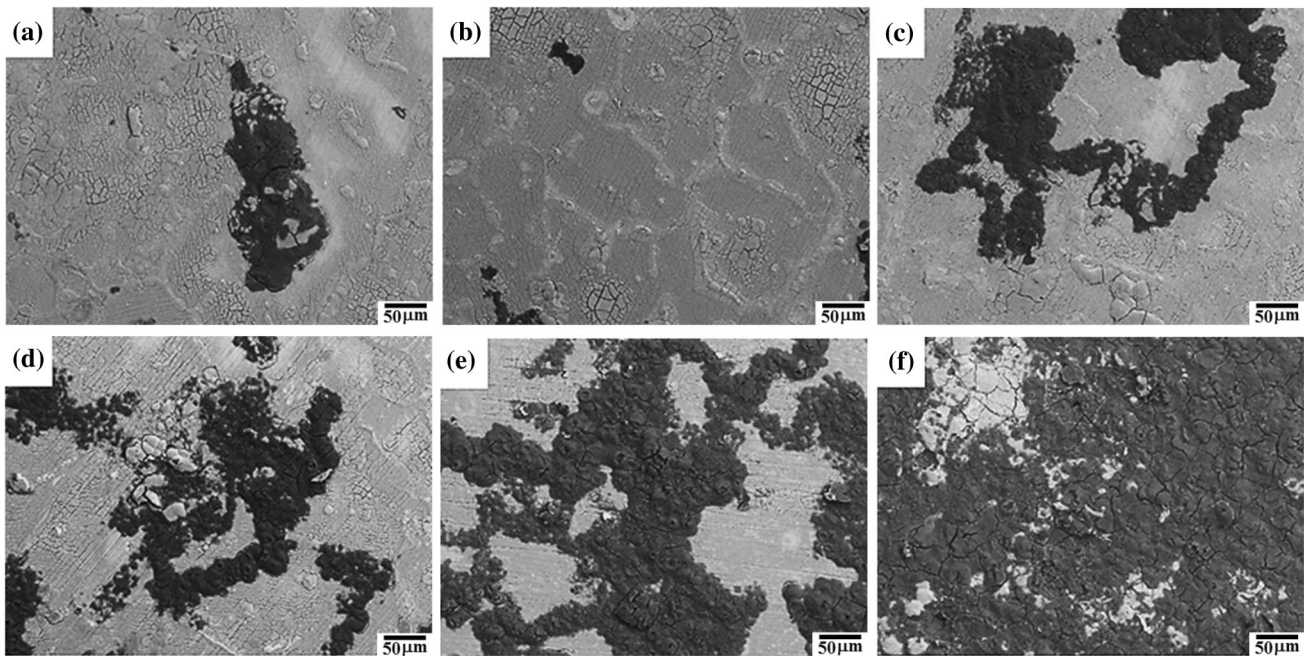
Fig. 6 SEM micrographs of (a) Mg-1.2Ca-1Zn and Mg-1.2Ca-1Zn-Bi alloys with various Bi content: (b) 0.5 wt.%, (c) 1.5 wt.%, (d) 3 wt.%, (e) 5 wt.% and (f) 12 wt.% after polarization in SBF at 37 °C
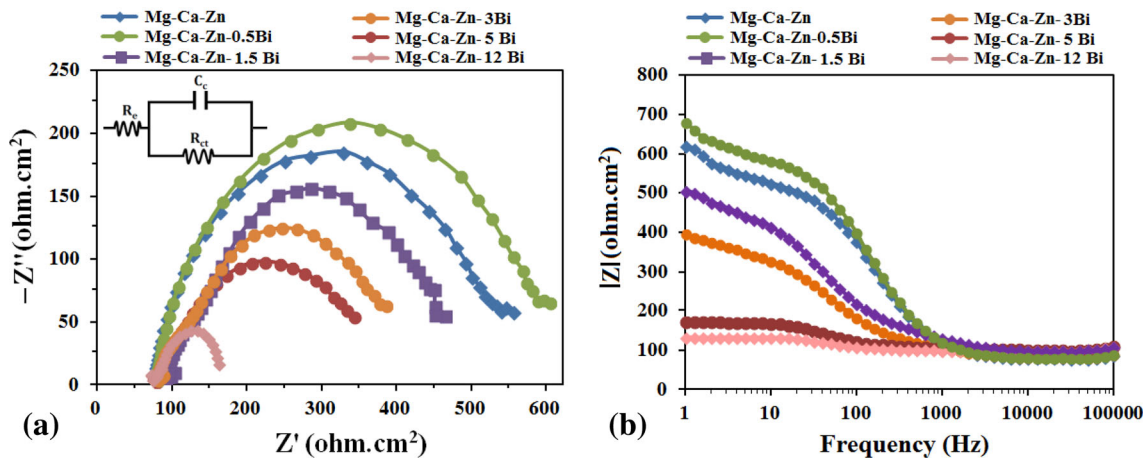

Fig. 7 Electrochemical impedance spectroscopy measurements of Mg-1.2Ca-1Zn and Mg-1.2Ca-1Zn-xBi alloys specimens in SBF at 37 °C (a) Nyquist plot and (b) Bode plot

protection property of the samples (Ref 36). It is clearly evident from the impedance value in the low-frequency range that the samples of Mg-1.2Ca-1Zn and Mg-1.2Ca-1Zn-0.5Bi alloys presented the best corrosion resistance as their values are the highest, $|Z|_{f=1Hz}$, 2.24×10^5 and 1.78×10^5 Hz, respectively. However, Mg-1.2Ca-1Zn-5Bi and Mg-1.2Ca-1Zn-12Bi alloys presented the lowest $|Z|_{f=1Hz}$ at the low-frequency limit (790 Hz) which was attributed to the precipitation of Mg_2Bi_2Ca phases and consequently formation of galvanic couple. Based on the result of electrochemical test, it is found that the corrosion behavior of Mg-1.2Ca-1Zn-xBi alloys is highly dependent on the amount and type of secondary phases formed.

3.3 Immersion Test

Figure 8 shows the surface morphologies of Mg-1.2Ca-1Zn and Mg-1.2Ca-1Zn-xBi alloys specimens after 168-h immersion in the Kokubo solution. Figure 8(a) and (b) shows that the entire surface of Mg-1.2Ca-1Zn alloy was covered by an insoluble corrosion product. The dehydration of the surface layer in the air has caused the formation of cracks on the surface of specimens. The presence of cracks allows the solution to have direct contact with the matrix and accelerating the corrosion process. The corrosion behavior of Mg-based alloys can be determined by observing the condition of the cracks and the surface. The degradation of Mg alloys in the SBF occurred according to the following equation:
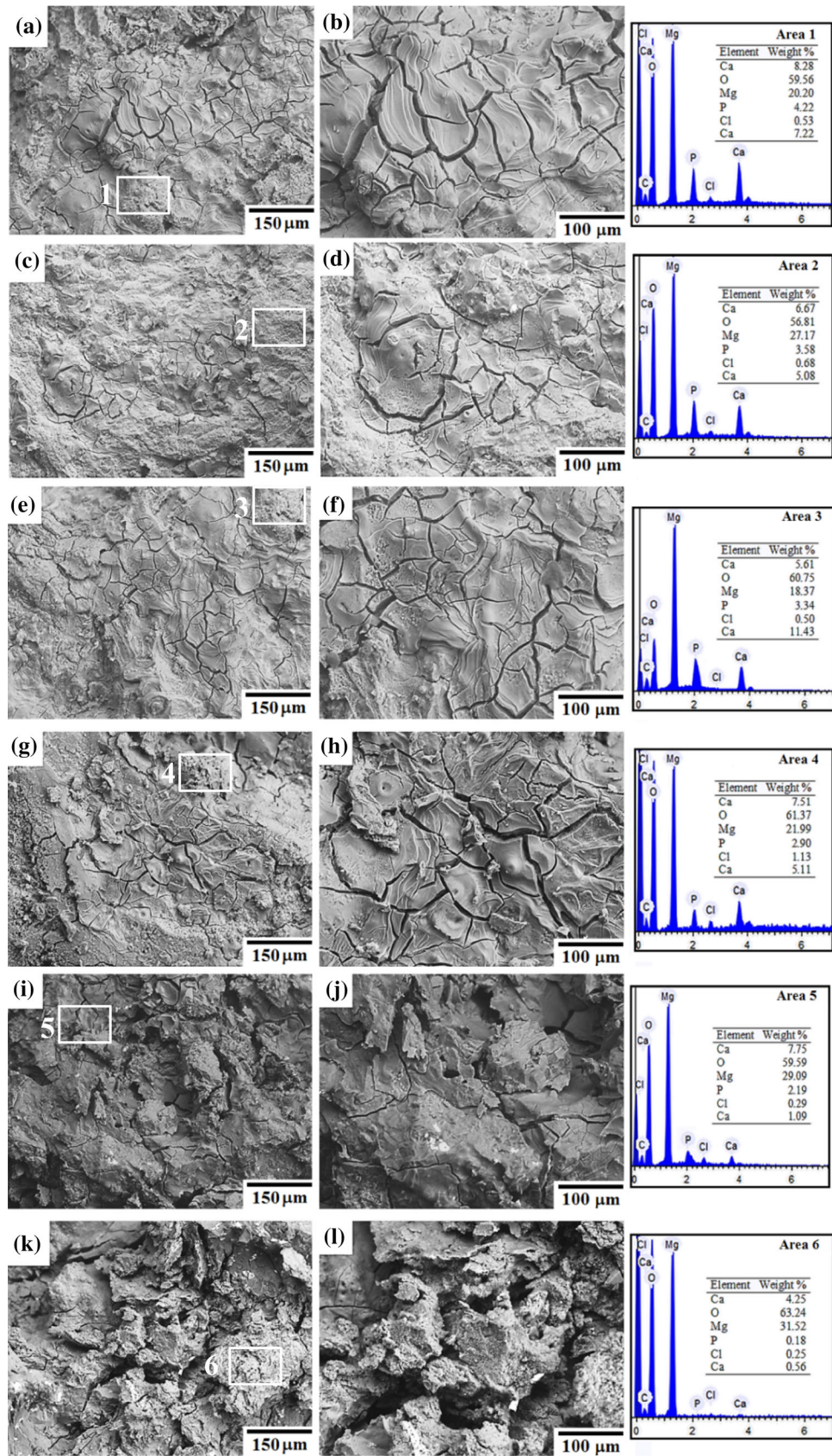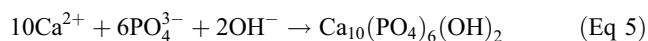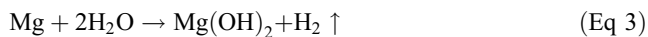
Fig. 8 SEM micrographs and corresponding EDX analysis of (a,b) Mg-1.2Ca-1Zn and Mg-1.2Ca-1Zn-Bi alloys with various Bi content: (c,d) 0.5, (e,f) 1.5, (g,h) 3, (i,j) 5 and (k,l) 12 wt.% after immersion in SBF for 168 h

$$Mg + 2H_2O \rightarrow Mg(OH)_2 + H_2 \uparrow \qquad (Eq\ 3)$$

$$Mg^{2+} + 2Cl^- \rightarrow MgCl_2 \qquad (Eq\ 4)$$

$$10Ca^{2+} + 6PO_4^{3-} + 2OH^- \rightarrow Ca_{10}(PO_4)_6(OH)_2 \qquad (Eq\ 5)$$

$Mg(OH)_2$ and H_2 will be produced when Mg-based alloy is immersed in SBF which is similar to the behavior of pure Mg (Eq 3). However, the existence of destructive $2Cl^-$ in the solution converted $Mg(OH)_2$ into a more soluble $MgCl_2$ (Eq 4). As the reaction progressed, hydroxyapatite $[Ca_{10}(PO_4)_6(OH)_2]$ would be formed due to the reaction between phosphate ions (HPO_4^{2-} or PO_4^{3-}) and Ca^{2+} in the solution with the OH^- (Eq 5). The surface of Mg-1.2Ca-1Zn-0.5Bi alloy (Fig. 8c, d) shows smaller cracks than Mg-1.2Ca-1Zn alloy which reflects that the improvement of corrosion resistance after addition of 0.5 wt.% of Bi into the alloy. Further addition of Bi content to 3 wt.%, these cracks became larger and deeper (Fig. 8e, f). The addition of Bi up to 12 wt.% has led to the formation of very rough surface and many large corrosion pits
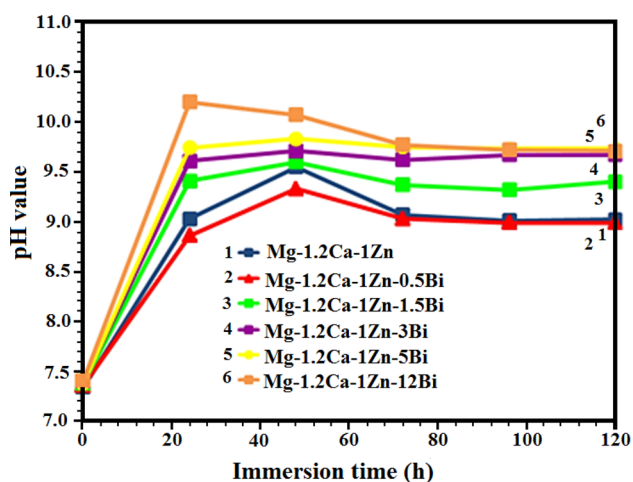

Fig. 9 Variation of the pH value in the Kokubo solution as a function of immersion time of the ternary Mg-1.2Ca-1Zn and quaternary Mg-1.2Ca-1Zn-xBi alloys with varying Bi content
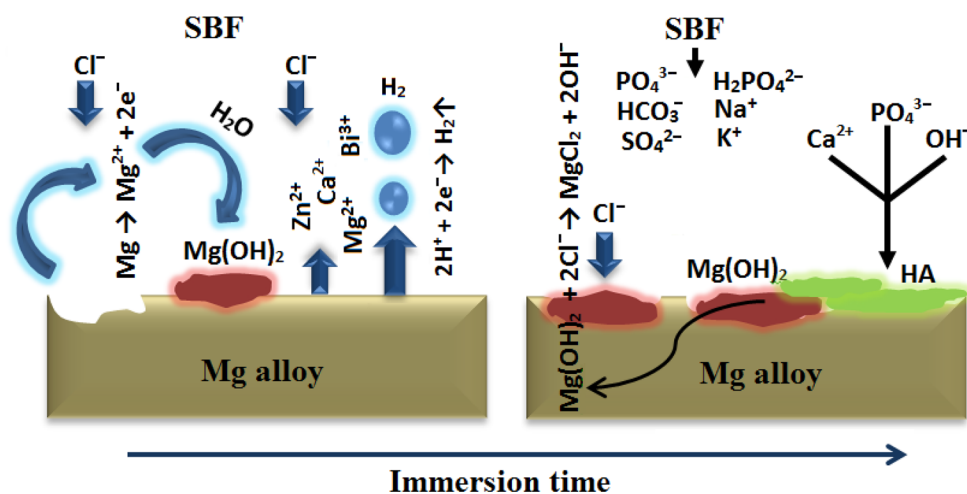
on the surface of the alloys. The EDS analysis revealed the presence of $Mg(OH)_2$ consistent with the atomic ratio of Mg to O (1:2). However, the EDS analysis of the corrosion layer indicates that the surface structure consist of Mg and O as well as traces amount of Ca and P, which represents the formation of HA. These micrographs and EDS results show that Mg-1.2Ca-1Zn-0.5Bi alloy has better corrosion behavior than Mg-1.2Ca-1Zn alloy. On the other hand, further addition of Bi up to 12 wt.% would deteriorate the corrosion resistance of Mg-1.2Ca-1Zn-xBi alloys. This is in good agreement with the result of polarization test.

Figure 9 shows the variation of the pH value for Mg-1.2Ca-1Zn-xBi alloys with different Bi contents in the Kokubo solution as a function of immersion time. Serious hemolysis could happen if the pH value of solution exceeds 10.2 for an implant (Ref 37). It can be observed that the pH values for all specimens increase significantly at the initial stage. According to Witte et al. (Ref 38), the increase in the pH value of solution was caused by the release of OH^- ions into the solution in the form of $Mg(OH)_2$ on the surface of specimens. The pH value then slightly decreased and became constant as immersion time increased because of the formation of $Mg(OH)_2$ and HA on the surface of the Mg-1.2Ca-1Zn-xBi alloys. The accumulation of corrosion products on the surface of the Mg alloy which can be function as protection layer to separate the substrate with the solution has caused the declination of pH value in the solution (Ref 39). Consequently, the corrosion behavior of alloys can be evaluated effectively by the variation of pH value as a function of immersion time (Ref 40). Thus, low pH value of solution indicates low corrosion rate of specimens. Mg-1.2Ca-1Zn-0.5Bi alloy shows the lowest slope compared to Mg-1.2Ca-1Zn and all other Mg-1.2Ca-1Zn-xBi alloys, indicating its excellent corrosion resistance. However, the corrosion rate of the specimens increased with a further increase in Bi from 1.5 up to 12 wt.%. This is due to the main role of Bi in the precipitation of the secondary phases which deteriorated the corrosion resistance of the alloys.

The corrosion mechanisms of the Mg-1.2Ca-1Zn-Bi alloy are schematically exhibited in Fig. 10. As bare Mg alloy was exposed to SBF solution, the grain boundaries preferentially corroded due to the microgalvanic activity between secondary phase and magnesium. Due to the occurrence of electrochemical reactions on the Mg alloy surface, a thin layer of $Mg(OH)_2$
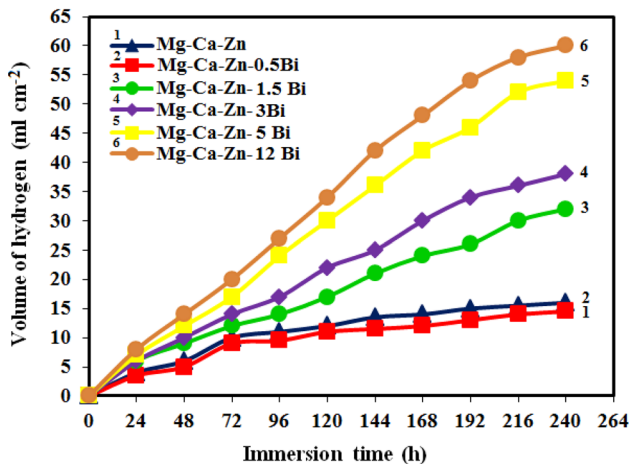

Fig. 10 Schematic illustration of the corrosion mechanism of Mg-1.2Ca-1Zn-Bi alloy

Fig. 11 Hydrogen evolution of the Mg-1.2Ca-1Zn and Mg-1.2Ca-1Zn-xBi alloys specimens after immersion in SBF solution for duration of 240 h

Fig. 12 X-ray diffraction patterns of (a) Mg-1.2Ca-1Zn and Mg-1.2Ca-1Zn-xBi alloys with varying Bi content (b) 0.5 wt.%, (c) 1.5 wt.%, (d) 3 wt.%, (e) 5 wt.% and (f) 12 wt.% after immersion in SBF solution for a duration of 168 h

was formed. However, due to the presence of Cl^- in the SBF solution, the $Mg(OH)_2$ will be transformed to more soluble $MgCl_2$ and release large amount of OH^- in the simulated physiological environment which resulted in significant increase in the pH value of the SBF solution. At the same time, the $MgCl_2$ dissolves to Mg^{2+} and $2Cl^-$ leaving several corrosion pits on the surface of the Mg alloy. As corrosion proceeded, by consuming Ca^{2+} and PO_3^{4-} from the physiological environment, hydroxyapatite (HA, $Ca_{10}(PO_4)_6(OH)_2$) precipitated on the $Mg(OH)_2$ which acted as nucleation template. With increasing immersion time, further magnesium alloy degraded and more HA precipitated on the Mg alloy surface which ended updecreasing the degradation rate of the Mg alloy. Zhang et al. (Ref [41]) exhibited that the precipitation of HA improved by degradation rate of magnesium alloy. However, Pan et al. (Ref [42]) demonstrated that alkaline solution and rough areas with large specific surface areas can promote nucleation sites for HA.

Figure 11 shows the cumulative volume of hydrogen produced by the Mg-1.2Ca-1Zn and Mg-1.2Ca-1Zn-12Bi alloy in SBF solution after different immersion times. The introduction of more than 0.5 wt.% bismuth into the ternary Mg-1.2Ca-1Zn alloy resulted in an increase in degradation rate in comparison with the ternary alloy. The hydrogen evolution was highest for the Mg-1.2Ca-1Zn-12Bi alloy, lowest for the Mg-1.2Ca-1Zn-0.5Bi and Mg-1.2Ca-1Zn alloys. The corresponding corrosion rates of Mg alloy containing 0.5, 1.5 and 3 wt.% Bi were calculated as 1.48, 3.13 and 3.73 ml/cm²/day, respectively, whereas it was 1.62 ml/cm²/day when Bi was not added. While Mg alloy containing 5 wt.% Bi and 12 wt.%, Bi exhibited fast corrosion rates of 5.43 ml/cm²/day and 6.04 ml/cm²/day, respectively. It can be also observed that the hydrogen production rapidly increased at the initial stage of the experiment due to the formation of thin and porous $Mg(OH)_2$ layer which is not able to protect Mg alloy against the penetration of the solution into the alloy. However, hydrogen production rate gradually decreases with increasing immersion time owing to the formation of a thicker and more corrosion products on the alloy surface leading to decline solution infiltration to the substrate hence reducing the hydrogen evolution (Ref [43]).
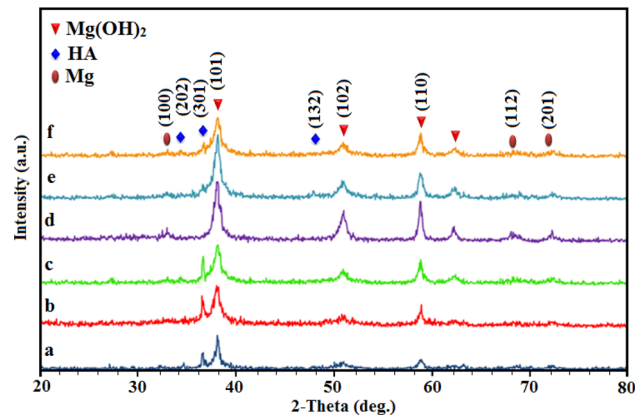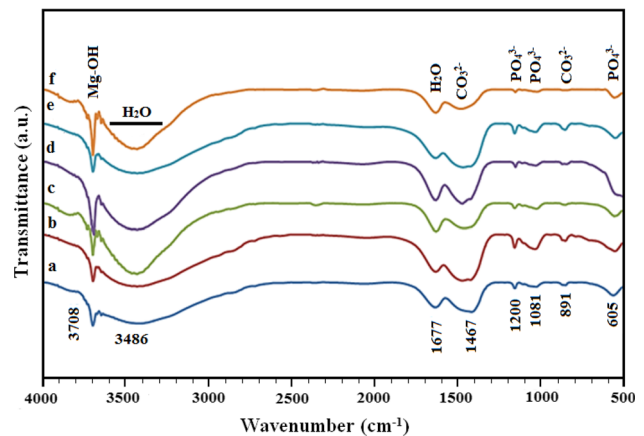

Fig. 13 FTIR results of (a) Mg-1.2Ca-1Zn and Mg-1.2Ca-1Zn-xBi alloys with varying Bi content (b) 0.5 wt.%, (c) 1.5 wt.%, (d) 3 wt.%, (e) 5 wt.% and (f) 12 wt.% after immersion in SBF for a duration of 168 h

Figure 12 shows the XRD diffraction patterns of the Mg-1.2Ca-1Zn and Mg-1.2Ca-1Zn-xBi alloys after immersion in Kokubo solution for 168 h. It shows the presence of $Mg(OH)_2$ reflections in addition to the reflections of HA and Mg. It can be seen that the diffraction of HA phases significantly increased with lower intensities of $Mg(OH)_2$ in Mg-1.2Ca-1Zn-0.5Bi alloy compared to Mg-1.2Ca-1Zn alloy. This result is in good agreement with the EDS analysis. It reflects that more protective films formed as the corrosion products on the surface of specimen. Both $Mg(OH)_2$ and HA appeared with different intensity reflections representing the influence of Bi content on corrosion behavior of specimens.

Fourier transform infrared (FTIR) spectrum of corrosion product of the Mg-1.2Ca-1Zn and Mg-1.2Ca-1Zn-xBi alloys after 168-h immersion in Kokubo solution is shown in Fig. 13. It can clearly be observed that the corrosion products formed on the surface of Mg-1.2Ca-1Zn and Mg-1.2Ca-1Zn-xBi alloys are similar but with different quantity. The O-H stretching vibration is observed at the peak of 3708 cm⁻¹ confirmed the formation of $Mg(OH)_2$. The bands at 3486 and 1677 cm⁻¹ are related to the water stretching vibration. The C-O stretching of the
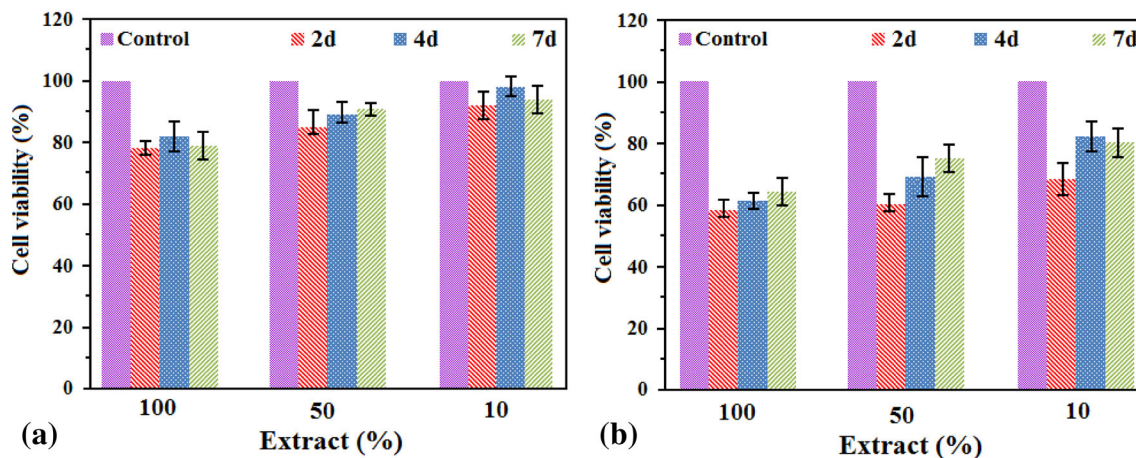
Fig. 14 Cell viability of MC3T3-E1 cells after incubation in a) Mg-1.2Ca-1Zn and b) Mg-1.2Ca-1Zn-0.5Bi alloys with extracts of three different 100, 50 and 10% concentration for 2, 4 and 7 days

carbonate groups is observed at 1467 and 891 cm^{-1} which represents the formation of HA. Phosphate groups (PO_4^{3-}) are detected at 1200, 1081 and 605 cm^{-1} after immersion for 168 h. The phosphate group can interrupt the action of chloride and reduce the dissolution rate of α-Mg.

3.4 Cytotoxicity Assessment

The Mg-1.2Ca-1Zn-0.5Bi alloy was selected for cytotoxicity test due to its lower degradation rate compared to the other alloys containing Bi. It was reported (Ref 44) that cells culture is an essential in vitro method in the cytocompatibility assessment of a new biomaterial. And cytotoxicity testing serves as a key indicator for quickly screening the biocompatibility of alloys; hence, it is vital to measure toxicity effect of the elements for biomedical application (Ref 45). Figure 14 shows the cell viability cultured in Mg-1.2Ca-1Zn and Mg-1.2Ca-1Zn-0.5Bi alloys extraction medium for 2, 4 and 7 days. In addition, the cell viability also increased with the increasing incubation time. Once diluting, the extracts into 50% and 10% the cell viabilities are all improved. The viability of MC3T3-E1 cells of the Mg-1.2Ca-1Zn-0.5Bi alloy was lower compared to that of control group, while the Mg-1.2Ca-1Zn alloy indicated slightly lower viability than that of control group. The results also revealed better cytocompatibility of Mg-5Zn-1Ca alloy to MC3T3-E1 cells than that of the Mg-1.2Ca-1Zn-0.5Bi alloy. Furthermore, ternary Mg-1.2Ca-1Zn alloy indicated higher cell viability than that of quaternary Mg-1.2Ca-1Zn-0.5Bi alloy. Similar study conducted by Zhang et al. (Ref 46) showed Mg-Zn alloys containing 1-3 wt.% also did not induce toxicity in cells. In this regard, Feyerabend et al. (Ref 47) investigated the in vitro cytotoxicity of the elements Y, Nd, Dy, Pr, Gd, La, Ce, Eu, Li and Zr and their results exhibited that the La and Ce have the highest cytotoxicity compared to the other elements. They also demonstrated that the cytotoxicity of these elements is strongly related to ionic radii. It should be noted that the ionic radius of Bi is similar to that of Ce element, indicating a relatively high cytotoxicity. However, Zhou et al. (Ref 48) investigated the in vitro cytocompatibility of binary Zr-1X (X = Ti, Nb, Mo, Cu, Au, Pd, Ag, Ru, Hf and Bi) after immersion in minimum essential medium (MEM) with 10% fetal bovine serum and their results exhibited no significant

difference between control group and Zr-1Bi alloys (Cell viability of 93%) indicating that the Zr-1Bi alloy is safe as an implantable material. Gao et al. (Ref 49) evaluated the cytotoxicity of bismuth oxychloride (BiOCl) nanosheets, and they indicated that BiOCl had no cytotoxicity at low concentrations (<0.5 µg/mL), while it shows toxic effects on HaCaT cells at higher concentrations (5-100 µg/mL). Other research (Ref 50) on bismuth revealed that Bi administrated orally is extracted from humans mainly in urine and feces. Sanderson et al. (Ref 51) reported no toxic effects of Bi shot embedded in the breast muscles of game-farm mallards. Therefore, results regarding the biocompatibility (Ref 52, 53) of Bi are contradictory and further investigations, including in vivo biocompatibility evaluations, are required to further understand and verify the biocompatibility of the magnesium alloy containing Bi.

4. Conclusion

The effect of different amount of Bi on the microstructure and in vitro corrosion behavior of Mg-1.2Ca-1Zn-xBi was investigated in a Kokubo simulated body fluid solution at 37 °C. The results indicate that addition of 0.5-12 wt.% Bi can effectively refine the grains of the Mg-1.2Ca-1Zn alloy. Three phases Mg$_2$Ca, Ca$_2$Mg$_6$Zn$_3$ and Mg$_3$Bi$_2$ were observed in Mg-1.2Ca-1Zn-xBi (x = 0.5, 1.5 and 3). However, in the Mg-1.2Ca-1Zn-xBi (x = 5 and 12), four different phases were identified; Mg$_2$Ca, Ca$_2$Mg$_6$Zn$_3$, Mg$_3$Bi$_2$ and Mg$_2$Bi$_2$Ca. Potentiodynamic polarization and EIS results exhibit that enhancement of the corrosion behavior of Mg-1.2Ca-1Zn alloy after addition of 0.5 wt.% Bi while further addition from 1.5 to 12 wt.% Bi significantly increases the corrosion rate of the ternary Mg-1.2Ca-1Zn alloy. Cytotoxicity test showed that Mg-1.2Ca-1Zn-0.5Bi alloy has a more toxic effect on MC3T3-E1 cells compared to Mg-1.2Ca-1Zn alloy. However, the Mg-1.2Ca-1Zn-0.5Bi alloy presented the best corrosion properties compared to Mg-1.2Ca-1Zn and other Mg-1.2Ca-1Zn-Bi alloys. Hence, it can be considered as an interesting candidate material for the development of biodegradable implants.

Acknowledgments

References

1. D. Tie, F. Feyerabend, N. Hort et al., In Vitro Mechanical and Corrosion Properties of Biodegradable Mg-Ag Alloys, *Mater. Corros.*, 2014, **65**, p 569–576

2. J. Zhou, Q. Li, H. Zhang, and F. Chen, Corrosion Behavior of AZ91D Magnesium Alloy in Three Different Physiological Environments, *J. Mater. Eng. Perform.*, 2014, **23**, p 181–186

3. S. Remennik, I. Bartsch, E. Willbold et al., New, fast corroding High Ductility Mg-Bi-Ca and Mg-Bi-Si Alloys, with No Clinically Observable Gas Formation in Bone Implants, *Mater. Sci. Eng. B*, 2011, **176**, p 1653–1659

4. F. Witte, V. Kaese, H. Haferkamp, E. Switzer et al., In Vivo Corrosion of Four Magnesium Alloys and the Associated Bone Response, *Biomaterials*, 2005, **26**, p 3557–3563

5. N.G. Wang, R.C. Wang, C.Q. Peng, and Y. Feng, Corrosion Behavior of Magnesium Alloy AP65 in 3.5% Sodium Chloride Solution, *J. Mater. Eng. Perform.*, 2012, **21**, p 1300–1308

6. H.R. Bakhsheshi-Rad, E. Hamzah, M. Daroonparvar et al., Fabrication and Corrosion Behavior of Si/HA Nano-composite Coatings on Biodegradable Mg-Zn-Mn-Ca Alloy, *Surf. Coat. Technol.*, 2014, **258**, p 1090–1099

7. X.N. Gu and Y.F. Zheng, A Review on Magnesium Alloys as Biodegradable Materials, *Front. Mater. Sci. China*, 2010, **4**, p 111–115

8. F. Witte and N. Hort, Degradable Biomaterials Based on Magnesium Corrosion, *Curr. Opin. Solid State Mater. Sci.*, 2008, **12**, p 63–72

9. H.R. Bakhsheshi-Rad, E. Hamzah, M. Daroonparvar et al., Bi-Layer Nano-TiO$_2$/FHA Composite Coatings on Mg-Zn-Ce Alloy Prepared by Combined Physical Vapour Deposition and Electrochemical Deposition Methods, *Vacuum*, 2014, **110**, p 127–135

10. G. Song, Control of Biodegradation of Biocompatable Magnesium Alloys, *Corros. Sci.*, 2007, **49**, p 1696–1701

11. M. Maguire and J. Cowan, Magnesium Chemistry and Biochemistry, *Biometals*, 2002, **15**, p 203–210

12. E. Ghali, W. Dietzel, and K.U. Kainer, General and Localized Corrosion of Magnesium Alloys: A Critical Review, *J. Mater. Eng. Perform.*, 2013, **22**, p 2875–2891

13. M.C. Lopes de Oliveira, V.S. Marques Pereira, O.V. Correa, and R.A. Antunes, Corrosion Performance of Anodized AZ91D Magnesium Alloy: Effect of the Anodizing Potential on the Film Structure and Corrosion Behavior, *J. Mater. Eng. Perform.*, 2014, **23**, p 593–603

14. H.R. Bakhsheshi-Rad, E. Hamzah, M.R. Abdul-Kadir, Safaa N. Saud, M. Kasiri-Asgarani, and R. Ebrahimi-Kahrizsangi, The Mechanical Properties and Corrosion Behavior of Double-Layered Nano Hydroxyapatite-Polymer Coating on Mg-Ca Alloy, *J. Mater. Eng. Perform.*, 2015, **24**, p 4010–4021

15. M. Daroonparvar, M.A. Mat Yajid, N.M. Yusof, H.R. Bakhsheshi-Rad, and E. Hamzah, Improvement of Corrosion Resistance of Binary Mg-Ca Alloys by Using Duplex Aluminum-Chromium Coatings, *J. Mater. Eng. Perform.*, 2015, **24**, p 2614–2627

16. D. Zander and N.A. Zumdick, Influence of Ca and Zn on the Microstructure and Corrosion of Biodegradable Mg-Ca-Zn alloys, *Corros. Sci.*, 2015, **93**, p 222

17. B.L. Mordike and T. Ebert, Magnesium: Properties—Applications—Potential, *Mater. Sci. Eng. A*, 2001, **302**, p 37–45

18. H.R. Bakhsheshi-Rad, E. Hamzah, S. Farahany, and M. Staiger, The Mechanical Properties and Corrosion Behavior of Quaternary Mg-6Zn-0.8Mn-xCa Alloys, *J. Mater. Eng. Perform.*, 2015, **24**, p 598–608

19. N. Kirkland, M. Staiger, D. Nisbet, C.J. Davies, and N. Birbilis, Performance-Driven Design of Biocompatible Mg Alloys, *JOM*, 2011, **63**, p 28–34

20. K. Hagihara, K. Fujii, A. Matsugaki, and T. Nakano, Possibility of Mg- and Ca-Based Intermetallic Compounds as New Biodegradable Implant Materials, *Mater. Sci. Eng. C*, 2013, **33**, p 4101–4111

21. W.C. Kim, J.G. Kim, J.Y. Lee, and H.K. Seok, Influence of Ca on the Corrosion Properties of Magnesium for Biomaterials, *Mater. Lett.*, 2008, **62**, p 4146–4148

22. H.R. Bakhsheshi-Rad, E. Hamzah, S.N. Saud, and M. Mamoun, Effect of Electrodeposition Parameters on the Microstructure and Corrosion Behavior of DCPD Coatings on Biodegradable Mg-Ca-Zn Alloy, *Int. J. Appl. Ceram. Technol.*, 2015, **12**, p 1054–1064

23. S. Cai, T. Lei, N. Li, and F. Feng, Effects of Zn on Microstructure, Mechanical Properties and Corrosion Behavior of Mg-Zn Alloys, *Mater. Sci. Eng. C*, 2012, **32**, p 2570–2577

24. W. Zhou, N.N. Aung, and Y. Sun, Effect of Antimony, Bismuth and Calcium Addition on Corrosion and Electrochemical Behaviour of AZ91 Magnesium Alloy, *Corros. Sci.*, 2009, **51**, p 403–408

25. J.M. Stellman, Encyclopedia of Occupational Health and Safety—4 Volume Set, 4th Edition/Edition 4, International Labour Organisation, 1998

26. Y.X. Wang, J.X. Zhou, J. Wang, T.J. Luo, and Y.S. Yang, Effect of Bi Addition on Microstructures and Mechanical Properties of AZ80 Magnesium Alloy, *Trans. Nonferr. Met. Soc. China*, 2011, **21**, p 711–716

27. T. Kokubo and H. Takadama, How Useful is SBF in Predicting In Vivo Bone Bioactivity?, *Biomaterials*, 2006, **27**, p 2907–2915

28. International Organization for Standardization, *ISO-10993-5: biological evaluation of medical devices part 5: tests for cytotoxicity: in vitro methods*, ANSI/AAMI, Arlington, VA, 2009

29. N.T. Kirkland, N. Birbilis, and J. Walker, In-Vitro Dissolution of Magnesium-Calcium Binary Alloys: Clarifying the Unique Role of Calcium Additions in Bioresorbable Magnesium Implant Alloys, *Biomed. Mater. Res. B*, 2010, **95B**, p 91–100

30. H.R. Bakhsheshi-Rad, M.R. Abdul-Kadir, M.H. Idris, and S. Farahany, Relationship Between the Corrosion Behavior and the Thermal Characteristics and Microstructure of Mg-0.5Ca-xZn Alloys, *Corros. Sci.*, 2012, **64**, p 184–197

31. L. Lu, A.K. Dahle, J.A. Taylor, and D.H. Stjohn, Theoretical and Practical Considerations of Grain Refinement of Mg-Al Alloys, *Mater. Sci. Forum*, 2005, **488-489**, p 299–302

32. N.S. Saud, E. Hamzah, T. Abubakar, H.R. Bakhsheshi-Rad, M. Zamri, and M. Tanemura, Effects of Mn Additions on the Structure, Mechanical Properties, and Corrosion Behavior of Cu-Al-Ni Shape Memory Alloys, *J. Mater. Eng. Perform.*, 2014, **23**, p 3620–3629

33. N.S. Saud, E. Hamzah, T. Abubakar, S. Farahany, and H.R. Bakhsheshi-Rad, Effects of Quenching Media on Phase Transformation Characteristics and Hardness of Cu-Al-Ni-Co Shape Memory Alloys, *J. Mater. Eng. Perform.*, 2015, **24**, p 1522–1530

34. X. Ye, S. Cai, Y. Dou et al., Bioactive Glass-Ceramic Coating for Enhancing the In Vitro Corrosion Resistance of Biodegradable Mg Alloy, *Appl. Surf. Sci.*, 2012, **259**, p 799–805

35. X. Lu, Y. Zuo, X. Zhao, Y. Tang, and X. Feng, The Study of a Mg-rich Epoxy Primer for Protection of AZ91D Magnesium Alloy, *Corros. Sci.*, 2011, **53**, p 153–160

36. M. Sababi, J. Pan, P.-E. Augustsson, P.-E. Sundell, and P.M. Claesson, Influence of Polyaniline and Ceria Nanoparticle Additives on Corrosion Protection of a UV-Cure Coating on Carbon Steel, *Corros. Sci.*, 2014, **84**, p 189–197

37. K.W. Guo, A Review of Magnesium/Magnesium Alloys Corrosion and Its Protection, *Recent Pat. Corros. Sci.*, 2010, **2**, p 13–21

38. F. Witte, A. Eliezer, and S. Cohen, The History, Challenges and the Future of Biodegradable Metal Implants, *Adv. Mat. Res.*, 2010, **95**, p 3–7

39. Q.F. Li, H.R. Weng, and Z.Y. Suo, Microstructure and Mechanical Properties of Bulk Mg-Zn-Ca Amorphous Alloys and Amorphous Matrix Composite, *Mater. Sci. Eng. A*, 2008, **487**, p 301–308

40. G. Manivasagam, D. Dhinasekaran, and A. Rajamanickam, Biomedical Implants: Corrosion and Its Prevention—A Review, *Recent Pat. Corros. Sci.*, 2010, **2**, p 40–54

41. S. Zhang, J. Li, Y. Song, C. Zhao, X. Zhang et al., In Vitro Degradation, Hemolysis and MC3T3-E1 Cell Adhesion of Biodegradable Mg-Zn Alloy, *Mater. Sci. Eng. C*, 2009, **29**, p 1907–1912

42. Y. Pan, S. He, D. Wang, D. Huang et al., In Vitro Degradation and Electrochemical Corrosion Evaluations of Microarc Oxidized Pure Mg, Mg-Ca and Mg-Ca-Zn Alloys for Biomedical Applications, *Mater. Sci. Eng. C*, 2015, **47**, p 85–96

43. M. Ascencio, M. Pekguleryuz, and S. Omanovic, An investigation of the Corrosion Mechanisms of WE43 Mg Alloy in a Modified Simulated Body Fluid Solution: The Influence of Immersion Time, *Corros. Sci.*, 2014, **87**, p 489–503

44. P. Yin, N.F. Li, T. Lei, L. Liu, and C. Ouyang, Effects of Ca on Microstructure, Mechanical and Corrosion Properties and Biocompatibility of Mg-Zn-Ca Alloys, *J. Mater. Sci. Mater. Med.*, 2013, **24**, p 1365–1373

45. Y. Chen, Z. Xu, C. Smith, and J. Sankar, Recent Advances on the Development of Magnesium Alloys for Biodegradable Implants, *Acta Biomater.*, 2014, **10**, p 4561–4573

46. B. Zhang, Y. Hou, X. Wang, Y. Wang, and L. Geng, Mechanical Properties, Degradation Performance and Cytotoxicity of Mg-Zn-Ca Biomedical Alloys with Different Compositions, *Mater. Sci. Eng. C*, 2011, **31**, p 1667–1673

47. F. Feyerabend, J. Fischer, J. Holtz, F. Witte et al., Evaluation of Short-Term Effects of Rare Earth and Other Elements Used in Magnesium Alloys on Primary Cells and Cell Lines, *Acta Biomater.*, 2010, **6**, p 1834–1842

48. F.Y. Zhou, K.J. Qiu, H.F. Li, T. Huang et al., Screening on Binary Zr-1X (X = Ti, Nb, Mo, Cu, Au, Pd, Ag, Ru, Hf and Bi) Alloys with Good In Vitro Cytocompatibility and Magnetic Resonance Imaging Compatibility, *Acta Biomater.*, 2013, **9**, p 9578–9587

49. X. Gao, X. Zhang, Y. Wang, Y. Wang, S. Peng, and C. Fan, An In Vitro Study on the Cytotoxicity of Bismuth Oxychloride Nanosheets in Human HaCaT Keratinocytes, *Food Chem. Toxicol.*, 2015, **80**, p 52–61

50. G.C. Sanderson, Acute Toxicity of Ingested Bismuth Alloy Shot in Game-Farm Mallards. Toxicity of Ingested Bismuth Alloy Shot in Game-Farm Mallards: Chronic Health Effects and Effects on Reproduction, Illinois Natural History Survey Bulletin, 1997

51. G.C. Sanderson, W.L. Anderson, C.L. Foley, L.M. Skowron, J.D. Brawn, and J.W. Seets, Acute Toxicity of Ingested Bismuth Alloy Shot in Game Farm Mallards, *Ill. Nat. Hist. Surv. Bull.*, 1997, **35**(3), p 185–216

52. M.R. Bafandeh, R. Gharahkhani, and M.H. Fathi, Fabrication, Characterization and Osteoblast Response of Cobalt-Based Alloy/Nano Bioactive Glass Composites, *J. Adv. Mater. Process.*, 2016, **4**, p 3–13

53. H.R. Bakhsheshi-Rad, E. Hamzah, S. Bagheriyan et al., Preparation and Performance of Plasma/Polymer Composite Coatings on Magnesium Alloy. *J. Mater. Eng. Perform.*, 2016, **25**, p 3948–3959